Supplementary Information

Single-Atom Platinum Sites with Asymmetric Coordination Environment on Fully Conjugated Covalent Organic Framework for Efficient Electrocatalysis

Zhang et al.

Results and Discussion

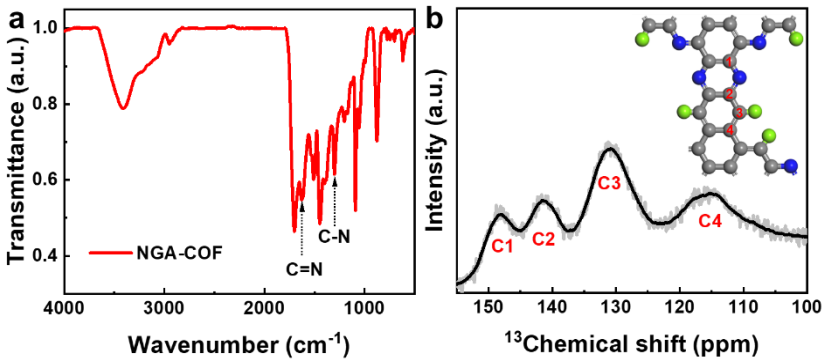

Supplementary Figure 1. (a) FTIR and (b) solid-state CP-MAS ^{13}C NMR spectra of NGA-COF.

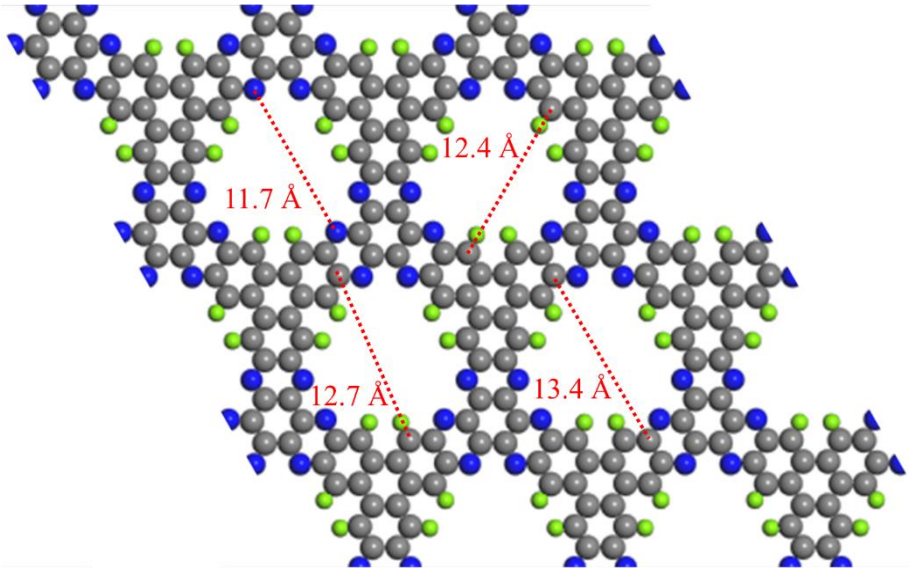

Supplementary Figure 2. (a) Simulated pore size of NGA-COF.

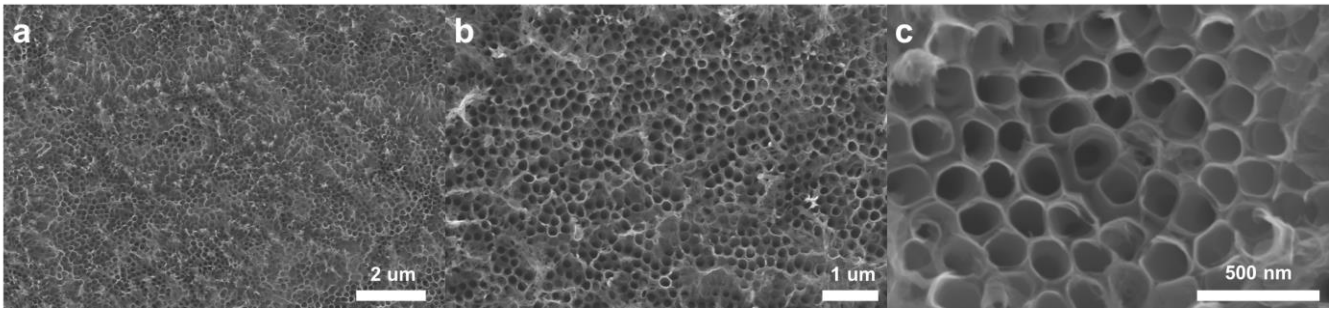

Supplementary Figure 3. (a-b) SEM images of TiO_2 NTs.

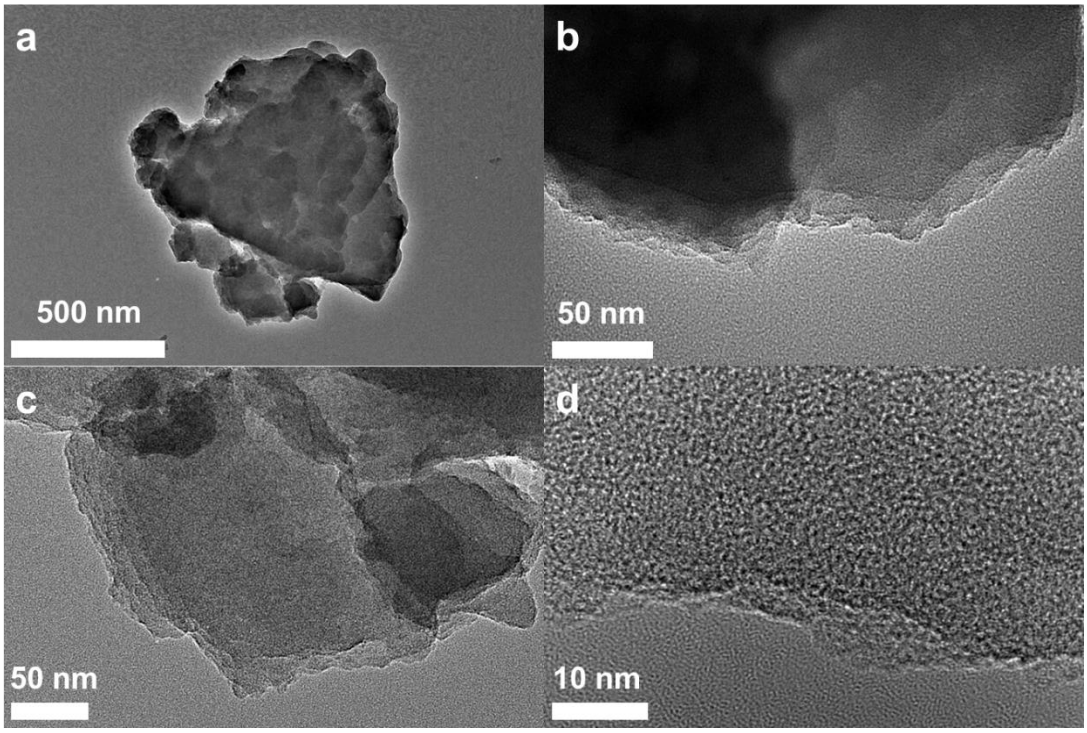

Supplementary Figure 4. (a-c) TEM and (d) HRTEM images of NGA-COF.

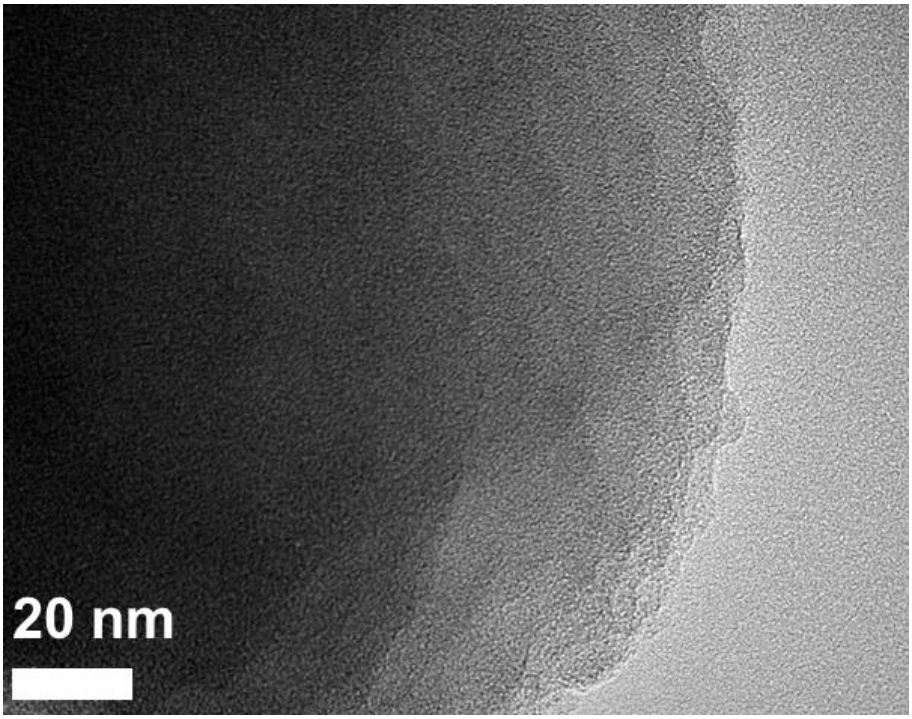

Supplementary Figure 5. HRTEM image of the edge of NGA-COF

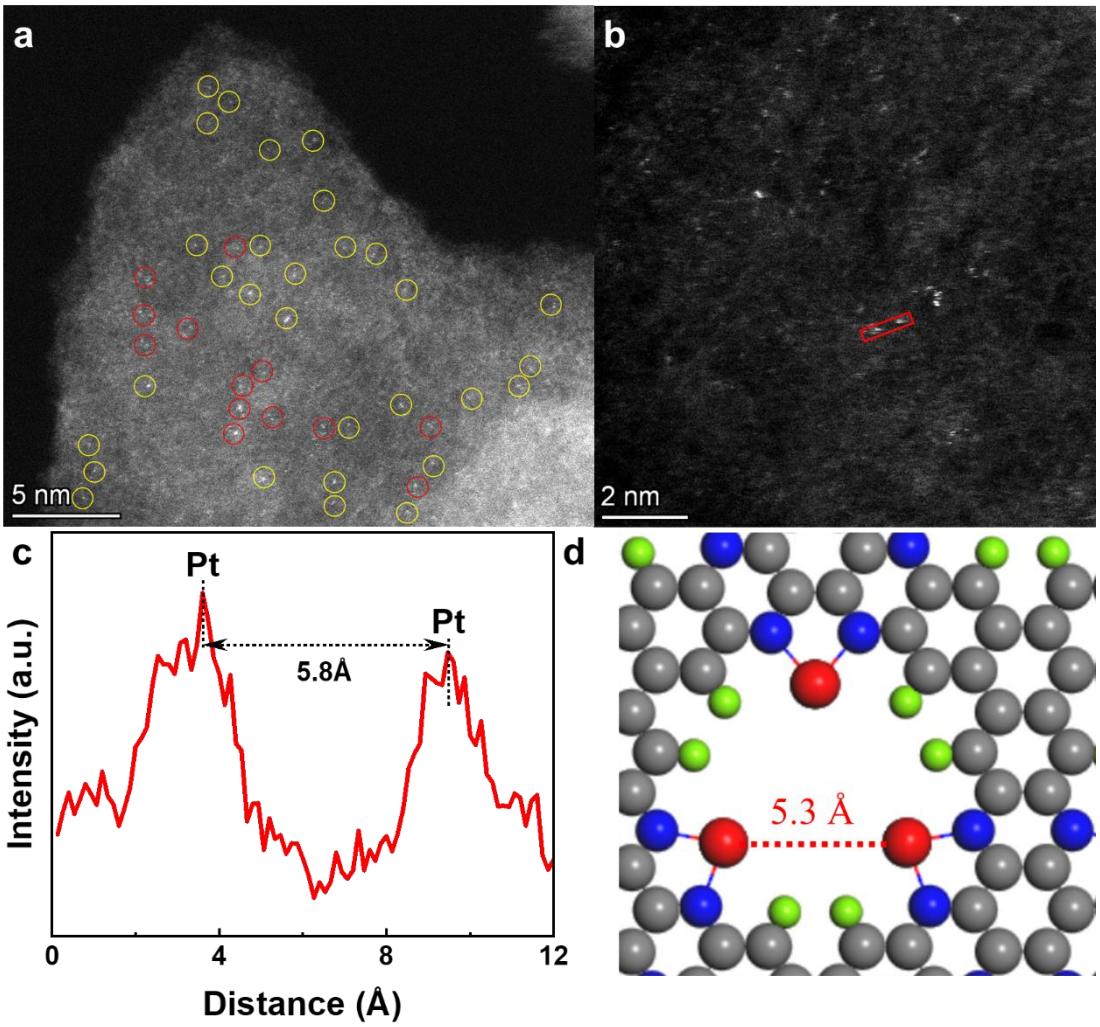

Supplementary Figure 6. (a) Magnified atomic-resolution HAADF-STEM image of NGA-COF@Pt. (b) Enlarged atomic-resolution HAADF-STEM image of NGA-COF@Pt and (c) corresponding distance between two bright spots (Pt atoms) in the red box. (d) Simulated distance between two adjacent Pt atoms in NGA-COF@Pt.

Notes for Supplementary Figure 6. Single atoms in the red circles of **Supplementary Figure 6a** mostly appear as atomic clusters, including diatomic or triatomic forms. Distance between the two atoms is about 5.8Å as observed in atomic-resolution HAADF-STEM at larger magnifications (**Supplementary Figure 6b-c**), which corresponds to the Pt space in the structure simulation (**Supplementary Figure 6d**).

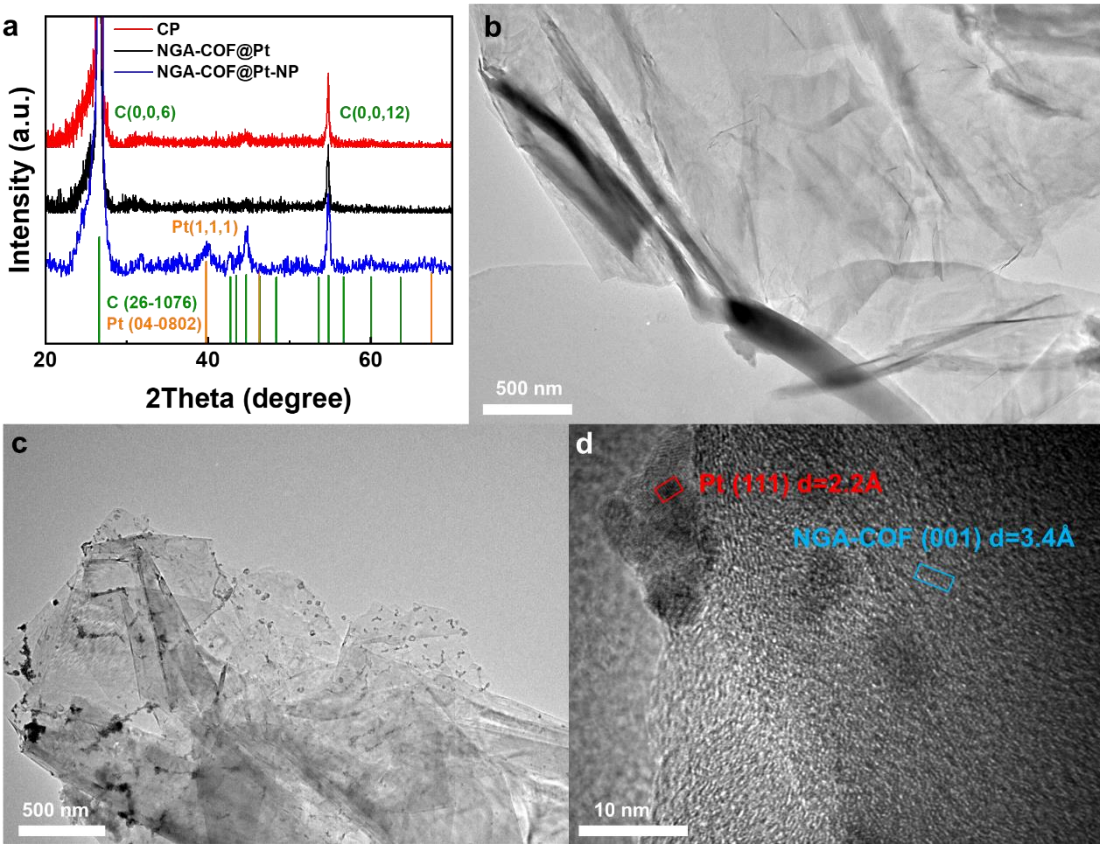

Supplementary Figure 7. (a) XRD patterns of NGA-COF@Pt on CP and bare CP. TEM images of (b) Nanosheets derived from NGA-COF@Pt after electrochemical modification, (c) NGA-COF@Pt-5000 and corresponding (d) HRTEM of NGA-COF@Pt-5000.

Note for Supplementary Figure 7: With the segment number of CV increasing from 2000 to 2500, typical Pt (111) peak emerges in X-ray diffraction (XRD) pattern (**Supplementary Figure 7a**). After electrochemical modification (2000 segments of CV), NGA-COF was exfoliated into nanosheets during the process[1], reducing the thickness of C-axis and the number of layers (**Supplementary Figure 7b**), which can increase the electrochemical active surface area (this will be proved later) of the catalyst and activate the catalytic sites originally buried deep inside NGA-COF. With the segment number of CV increasing to 2500, Pt particles on NGA-COF@Pt-NP were observed by TEM (**Supplementary Figure 7c**). Despite electrodeposition under acidic conditions (0.5 M H_2SO_4) for more than 24 h, the (001) crystal plane of NGA-COF and the layered graphene-like structure along C-axis remain. Such high stability can be attributed to the highly π–π conjugated multiring aromatic systems of NGA-COF (**Supplementary Figure 7d**).

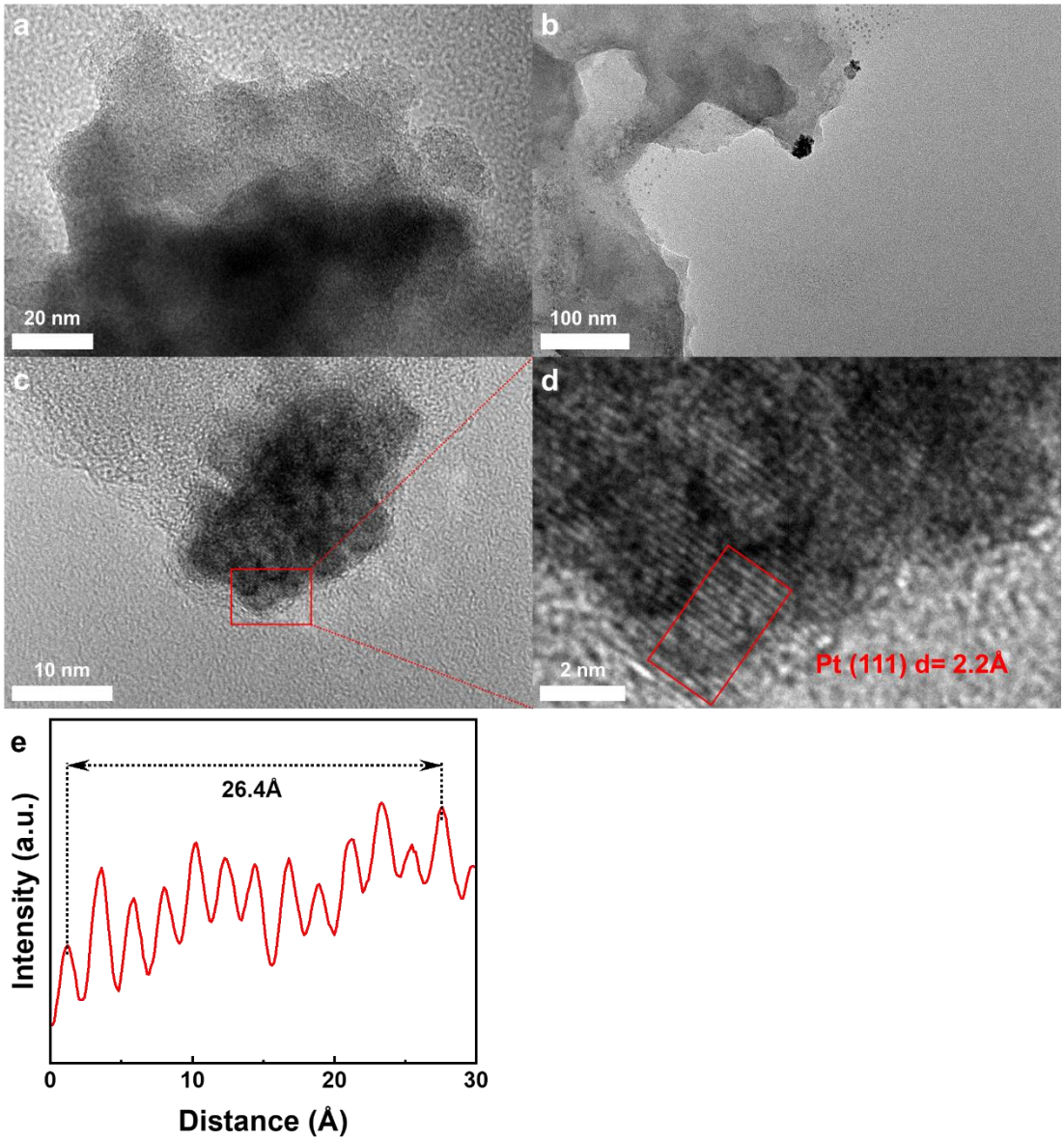

Supplementary Figure 8. TEM images of (a) NGA-COF@Pt (2000 segments of CV) and (b) NGA-COF@Pt-NP (2500 segments of CV). (c-d) Magnified HRTEM images of NGA-COF@Pt-NP. (e) Corresponding lattice spacing in the red box of **Supplementary Figure 8d**.

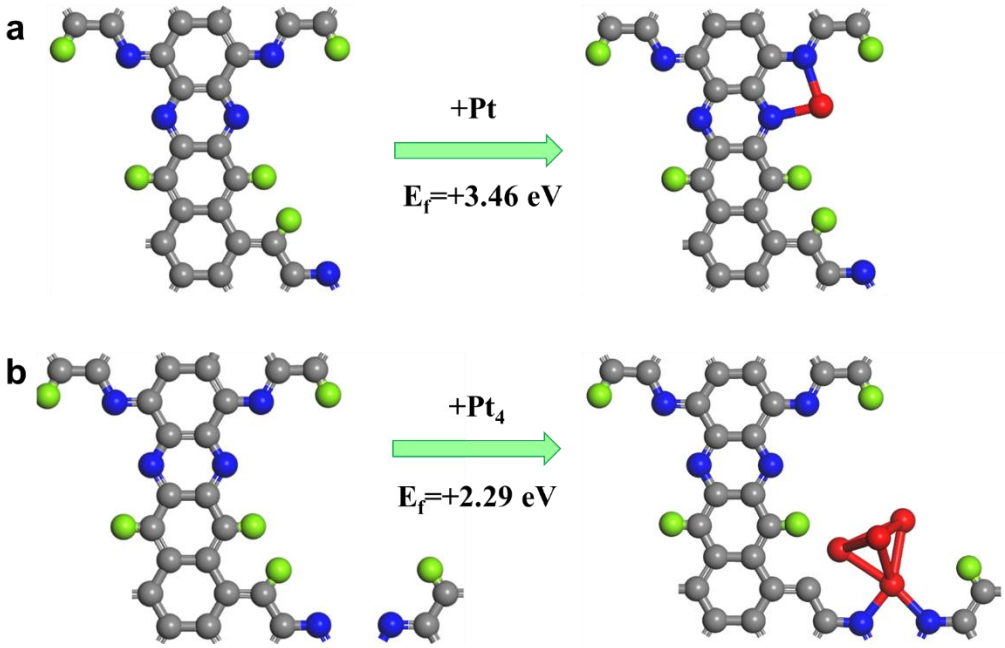

Supplementary Figure 9. Reaction path and formation energy of (a) NGA-COF@Pt and (b) NGA-COF@Pt-NP.

Note for Supplementary Figure 9: Although NGA-COF@Pt-NP is more thermodynamically stable than NGA-COF@Pt theoretically, the formation energy of these two structures is too high (3.46 eV for NGA-COF@Pt and +2.29 for NGA-COF@Pt-NP) for them to form at normal temperature and pressure spontaneously. Therefore, electrochemical modification synthetic method was applied to overcome the activation energy barrier required for the forming of Pt single atoms on NGA-COF. This method can control the reaction process by adjusting specific and quantifiable parameters such as voltage, current and deposition time. Furthermore, a general electrochemical modification strategy has also been developed to prepare conductive agent-free COF-based electrocatalysts at room temperature and pressure, which will not waste a large amount of solution containing noble metal ions due to subsequent processes such as centrifugation and filtration as liquid-phase or hydrothermal synthesis[2,3]. Besides, the mild electrochemical synthesis method can also avoid the agglomeration of single atom sites due to excessive surface energy at high temperatures as in the traditional pyrolysis method[4]. Such a controllable, facile and low-cost electrochemical modification method can dramatically reduce the waste of noble metals by minimizing the usage of Pt during the whole synthesis process.

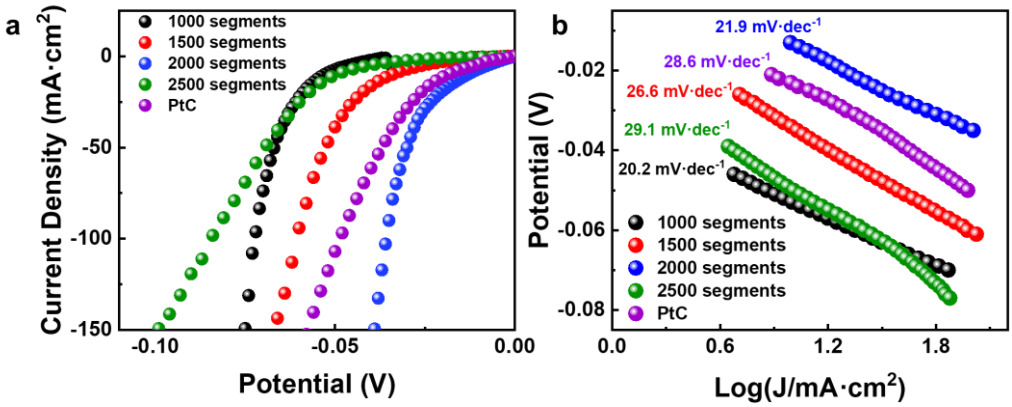

Supplementary Figure 10. (a) Polarization curves and (b) corresponding Tafel plots of NGA-COF@Pt after electro-deposition for different segments.

Note for Supplementary Figure 10: It can be concluded that CV for 2000 segments is the best electrochemical modification parameter to form NGA-COF@Pt among all the samples tested above. When the segments are less than 2000, the occupation of Pt single atoms into NGA-COF is not adequate, whereas when the CV is more than 2000 segments, Pt particles will be formed, resulting in the decrease of active sites and the degradation of catalytic performance.

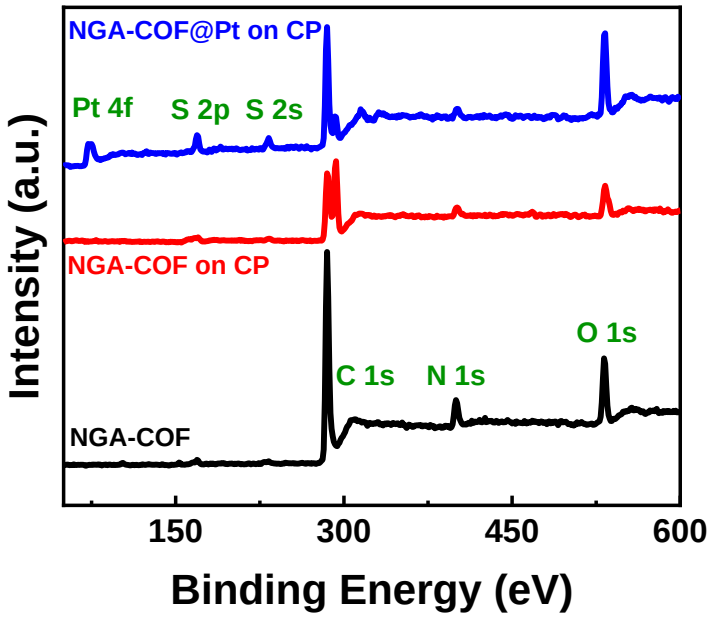

Supplementary Figure 11. (a) XPS survey spectra of different samples.

Note for Supplementary Figure 11: The full spectrum in **Supplementary Figure 11** confirms the introduction of Pt after electrochemical modification.

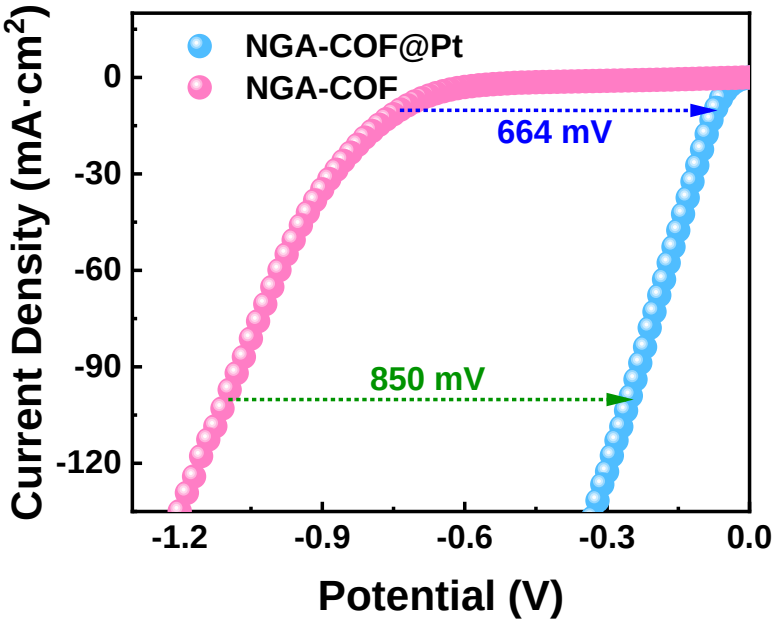

Supplementary Figure 12. Polarization curves of NGA-COF and NGA-COF@Pt without iR-compensation in 0.5 M H_2SO_4

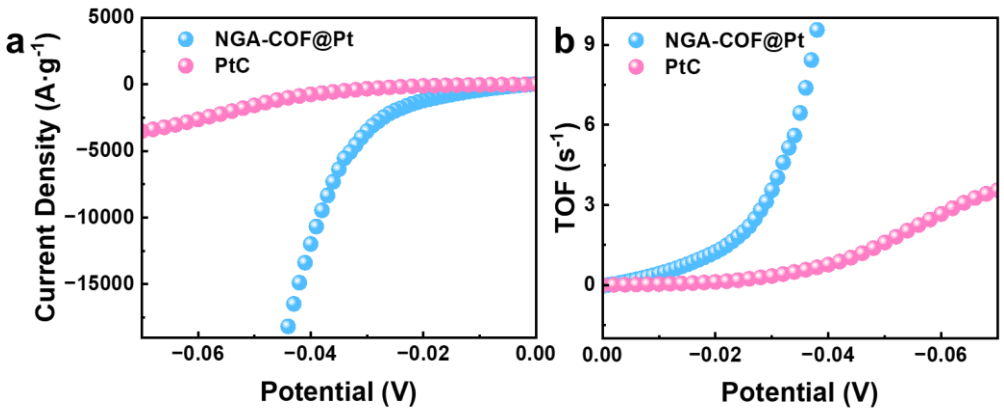

Supplementary Figure 13. (a) Mass activity and (b) TOF plotted as a function of the potential for NGA-COF@Pt and PtC in 0.5 M H_2SO_4.

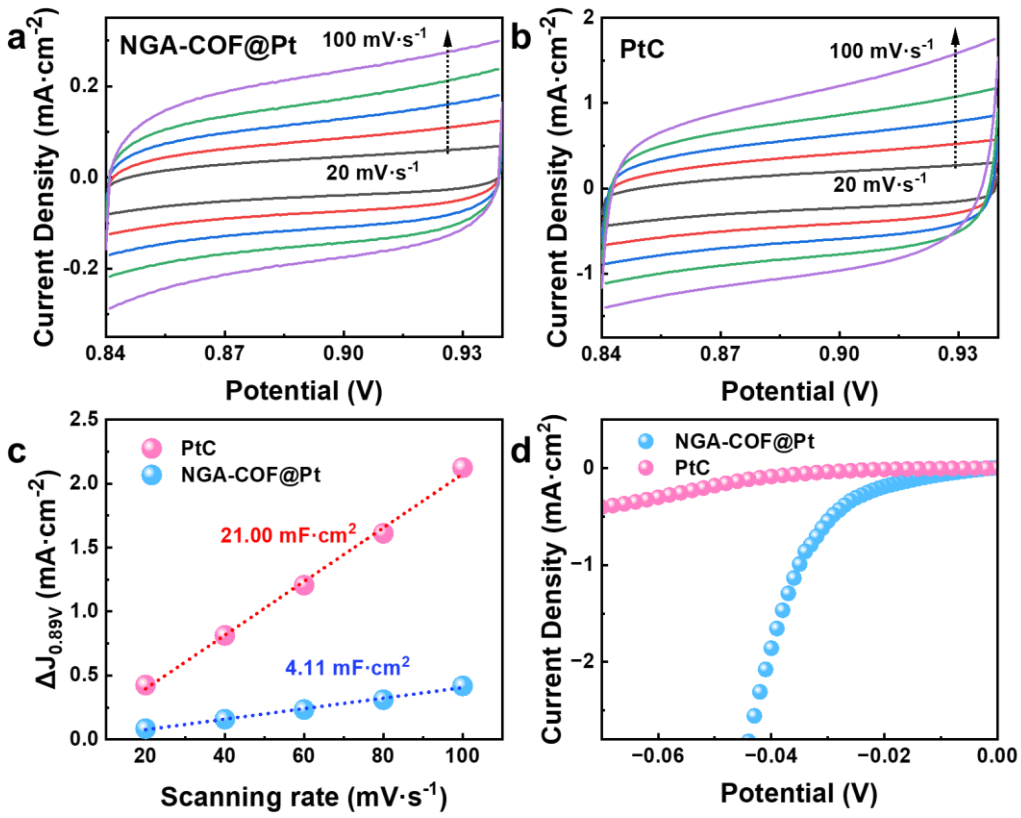

Supplementary Figure 14. CV curves of (a) NGA-COF@Pt and (b) PtC in different scanning rates. (c) C_{dl} calculated with ΔJ at 0.89 V. (d) Polarization curves normalized by ECSA. Electrolyte: 0.5 M H_2SO_4.

Notes for Supplementary Figure 14: ECSA is estimated by CVs with ECSA = C_{dl}/C_s (C_{dl} is double layer capacitance, C_s is capacitive behavior)[5]. The specific capacitance can be converted into ECSA using an average C_s value of 40 μF·cm^{-2} according to literature[6]. Therefore, ECSA of PtC and NGA-COF@Pt can be calculated to be 525.0 and 102.8 cm^2 in 0.5 M H_2SO_4.

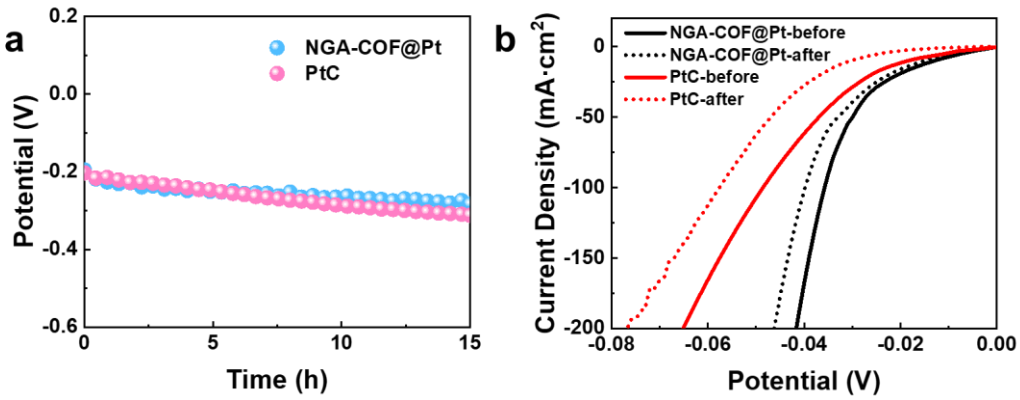

Supplementary Figure 15. Chronopotentiometric tests and (b) corresponding polarization curves of different samples before and after chronopotentiometric tests in 0.5 M H_2SO_4.

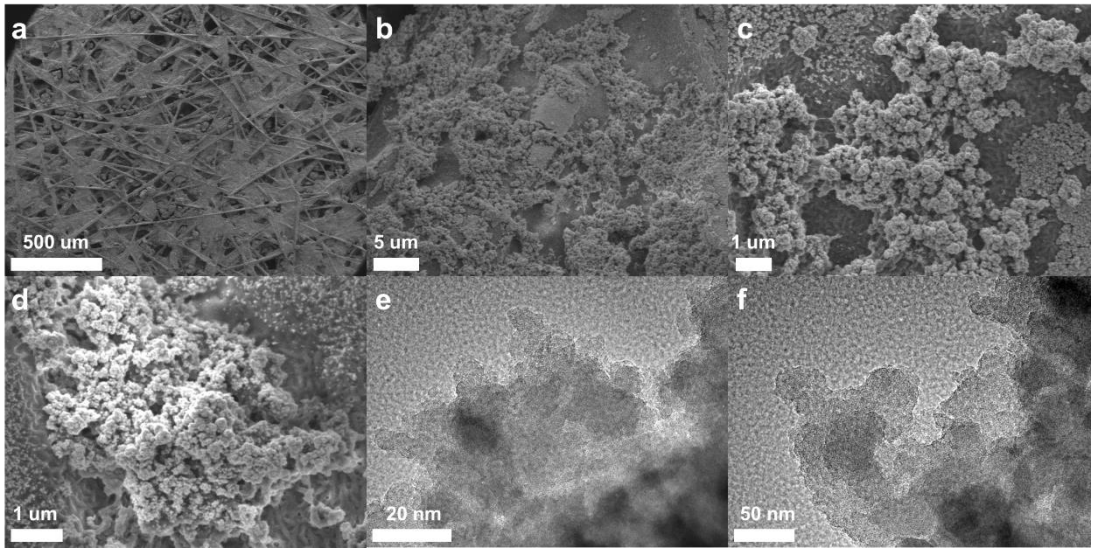

Supplementary Figure 16. (a-d) SEM images and (e-f) TEM images at different magnifications of NGA-COF@Pt after chronopotentiometric test in 0.5 M H_2SO_4.

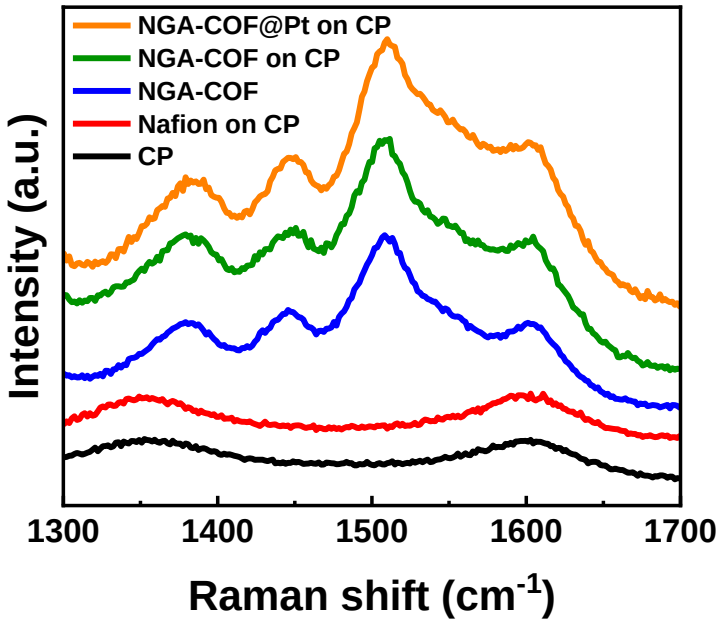

Supplementary Figure 17. Ex-situ Raman spectra of different samples prior to electrochemical tests.

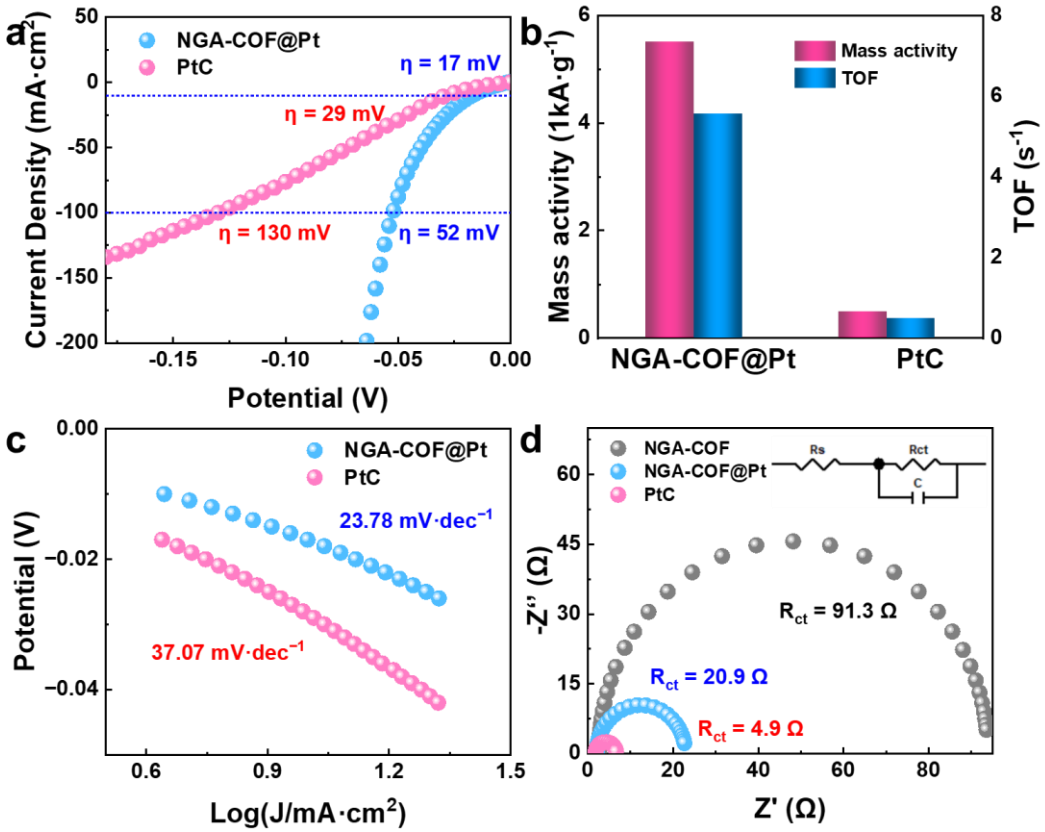

Supplementary Figure 18. (a) Polarization curves, (b) mass activity and TOF, (c) corresponding Tafel plots and (d) EIS of different samples in 1 M KOH.

Notes for Supplementary Figure 18: NGA-COF@Pt exhibits lower overpotential (19 mV) at 10 $mA \cdot cm^{-2}$ than PtC (**Supplementary Figures 18a and 19**). It also demonstrates outstanding mass activity and TOF (5502 $A \cdot g^{-1}$ and 5.56 s^{-1}) at overpotential of 50 mV, more than ten times than that of PtC (486 $A \cdot g^{-1}$ and 0.49 s^{-1}), surpassing that of noble metal materials reported recently (**Supplementary Figures 18b, 20 and Table 4**), too. Besides, NGA-COF@Pt also possesses lower Tafel slop (23.78 mV dec^{-1}, **Supplementary Figure 18c**), smaller electron transfer resistance (20.9 Ω, **Supplementary Figure 18d**), higher ECSA normalized current density (**Supplementary Figure 21**) and better stability (**Supplementary Figure 22**). Interestingly, after the stability test, the particle size of NGA-COF@Pt under alkaline conditions still remained almost original (**Supplementary Figure 23**) while it reduced under acidic conditions (**Supplementary Figure 16**). It is possible that imine bonds are more stable in alkaline than acidic conditions[7], resulting in the decrease of the polymerization degree of NGA-COF@Pt under acidic conditions.

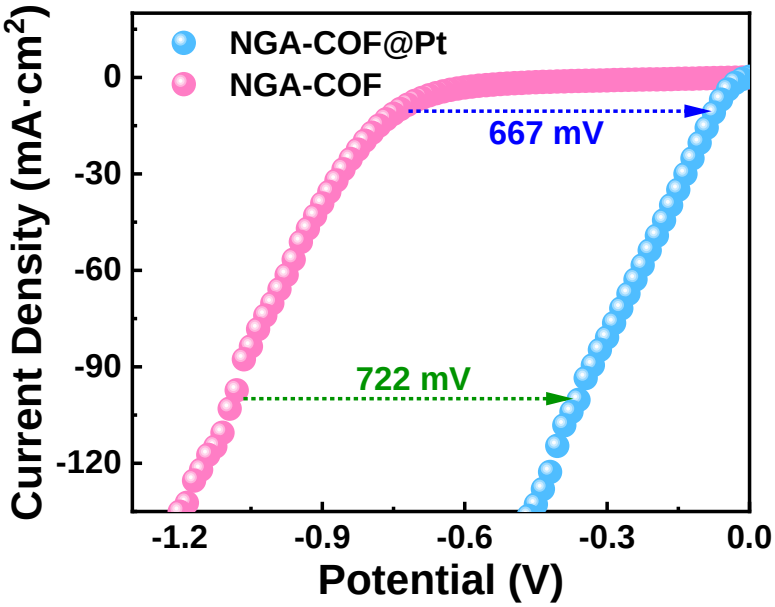

Supplementary Figure 19. Polarization curves of NGA-COF and NGA-COF@Pt without iR-compensation in 1 M KOH.

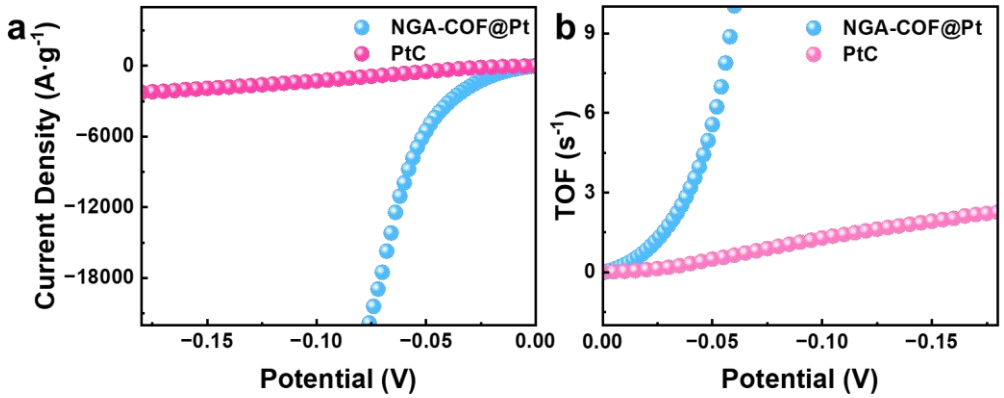

Supplementary Figure 20. (a) Mass activity and (b) TOF plotted as a function of potential for NGA-COF@Pt and PtC in 1 M KOH.

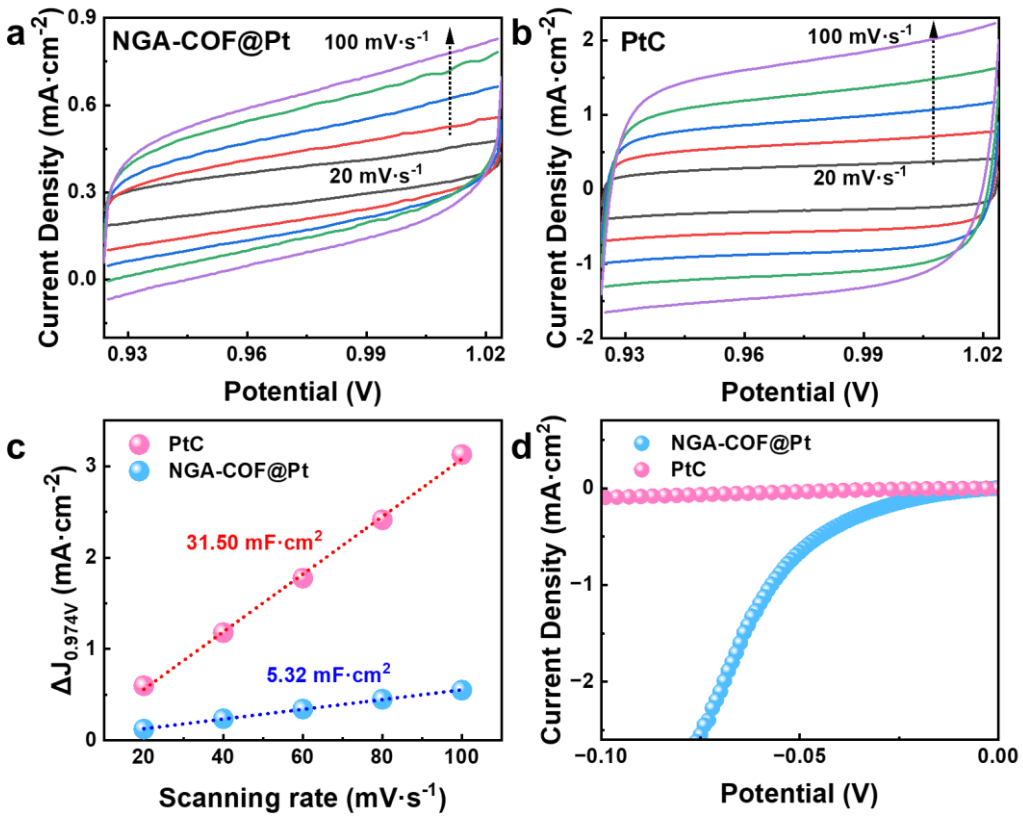

Supplementary Figure 21. CV curves of (a) NGA-COF@Pt and (b) PtC in different scanning rates. (c) C_{dl} calculated with ΔJ at 0.974 V. (d) Polarization curves normalized by ECSA. Electrolyte: 1 M KOH.

Notes for Supplementary Figure 21. The ECSA of PtC and NGA-COF@Pt is calculated to be 787.5 and 133.0 cm^2 in 1 M KOH.

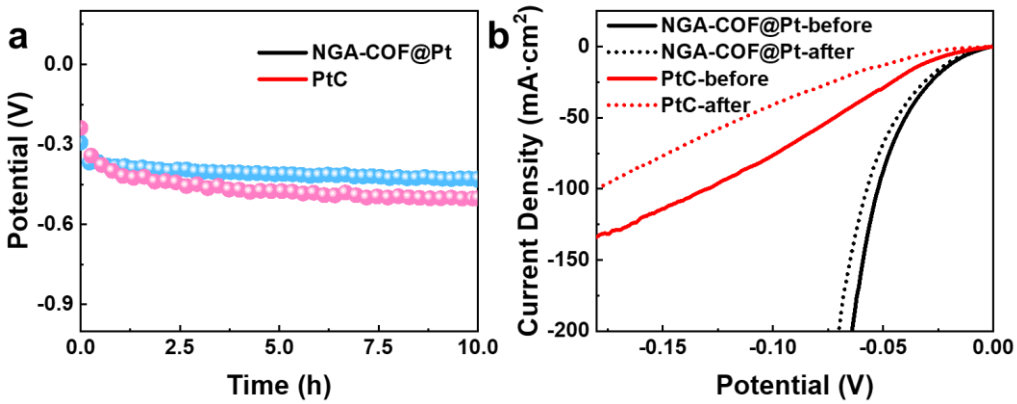

Supplementary Figure 22. Chronopotentiometric tests and (b) corresponding polarization curves of different samples prior to and after chronopotentiometric tests in 1 M KOH.

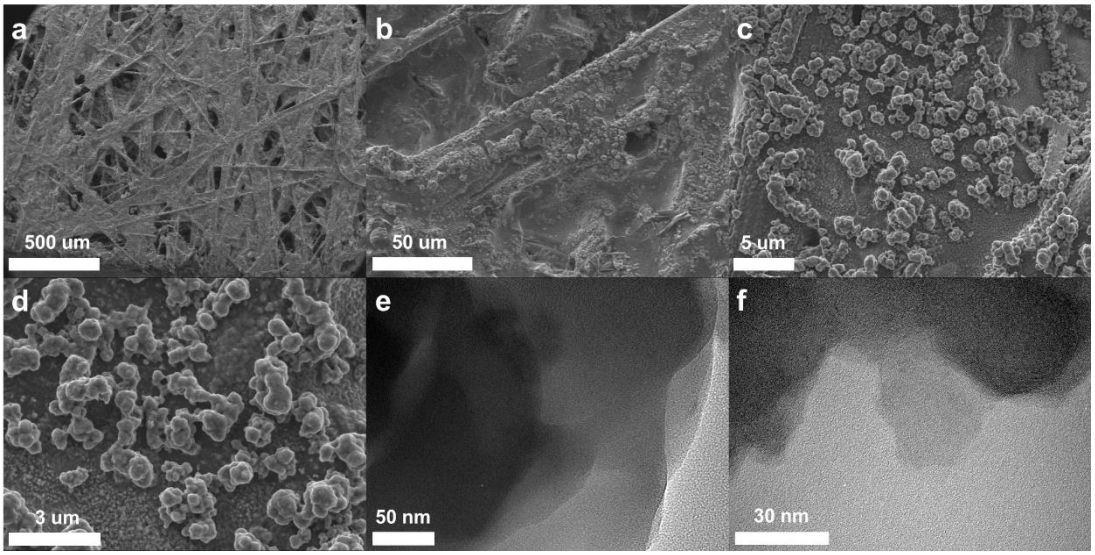

Supplementary Figure 23. (a-d) SEM images and (e-f) TEM images at different magnifications of NGA-COF@Pt after chronopotentiometric tests in 1 M KOH.

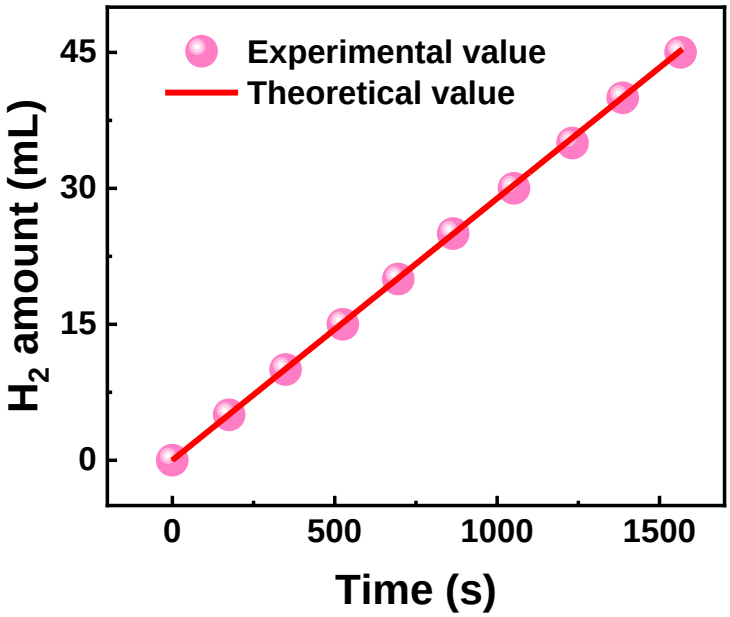

Supplementary Figure 24. Experimental and theoretical value of H_2 production by using NGA-COF@Pt as working electrode. (FE = 99.53%)

Notes for Supplementary Figure 24: Catalytic efficiency was tested by a home-made drainage device and a Faraday efficiency (FE) of 99.53 % was obtained.

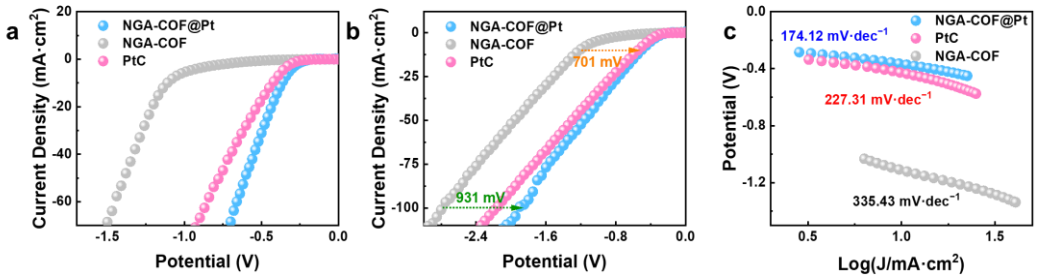

Supplementary Figure 25. Polarization curves (a) with or (b) without iR-compensation and (c) corresponding Tafel plots of NGA-COF, NGA-COF@Pt, PtC in 0.1 M PBS (pH 7.4).

Notes for Supplementary Figure 25: In addition, the electrochemical performance of NGA-COF@Pt towards HER in a neutral environment (0.1 M PBS, pH 7.4) was also recorded. LSV curves were collected in 0.1 M PBS (pH 7.4) solution with saturated calomel electrode (SCE) used as RE ($E_{RHE} = E_{SCE} + 0.241 + 0.059$ pH). Although the overpotential needed for NGA-COF@Pt (368 mV) to achieve 10 mA·cm^{-2} is lower than that of commercial PtC (429 mV), this value is still far from practical applications. Therefore, there is room for the improvement and optimization of the catalytic performance of NGA-COF@Pt towards HER under neutral conditions.

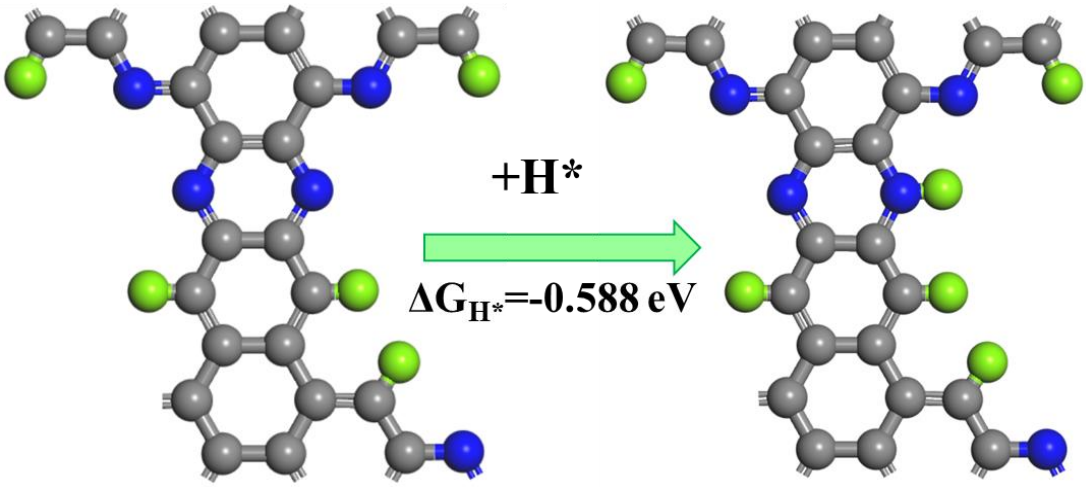

Supplementary Figure 26. Configurations of H* intermediate adsorbed on the N site of NGA-COF.

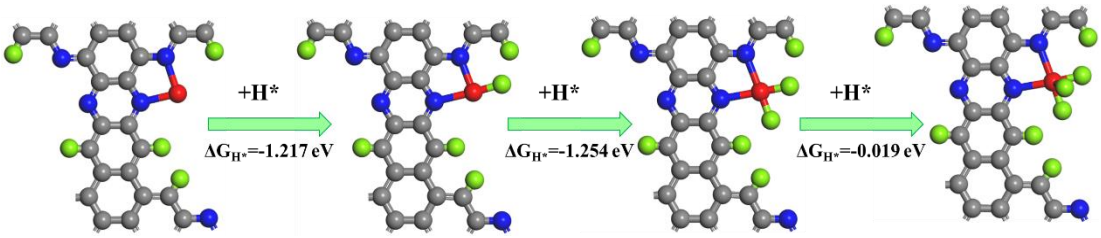

Supplementary Figure 27. Configurations of H* intermediate adsorbed on the Pt site of NGA-COF@Pt, NGA-COF@Pt-H and NGA-COF@Pt-2H, respectively.

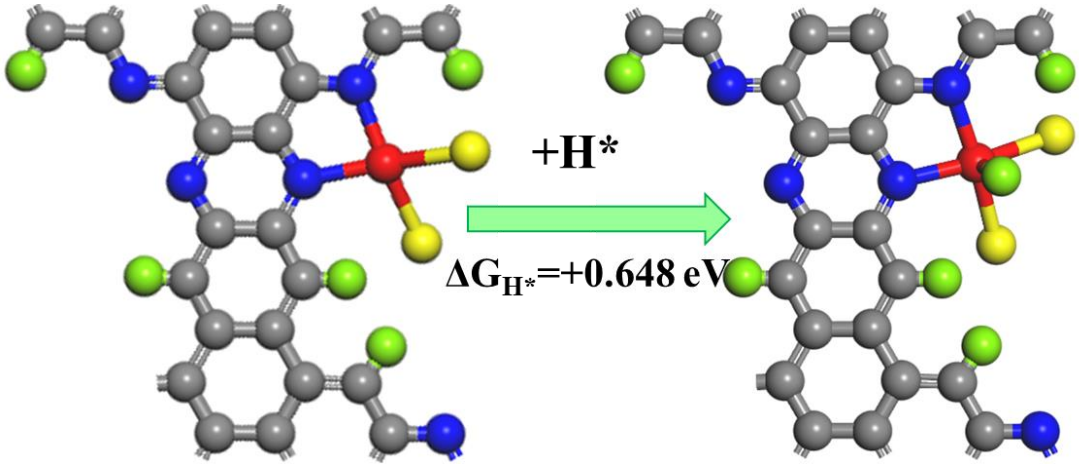

Supplementary Figure 28. Configurations of H* intermediate adsorbed on the Pt site of NGA-COF@Pt-2Cl.

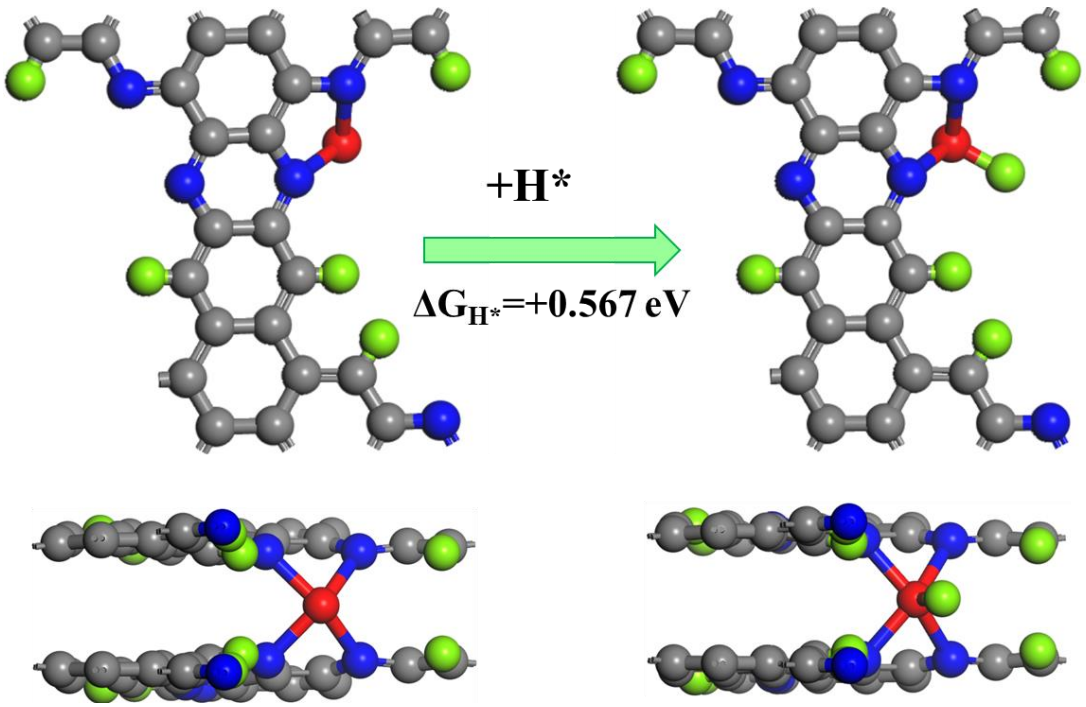

Supplementary Figure 29. Configurations of H* intermediate adsorbed on the Pt site of NGA-COF@Pt-N_4 alone C (the top two pictures) and B axis (the bottom two pictures).

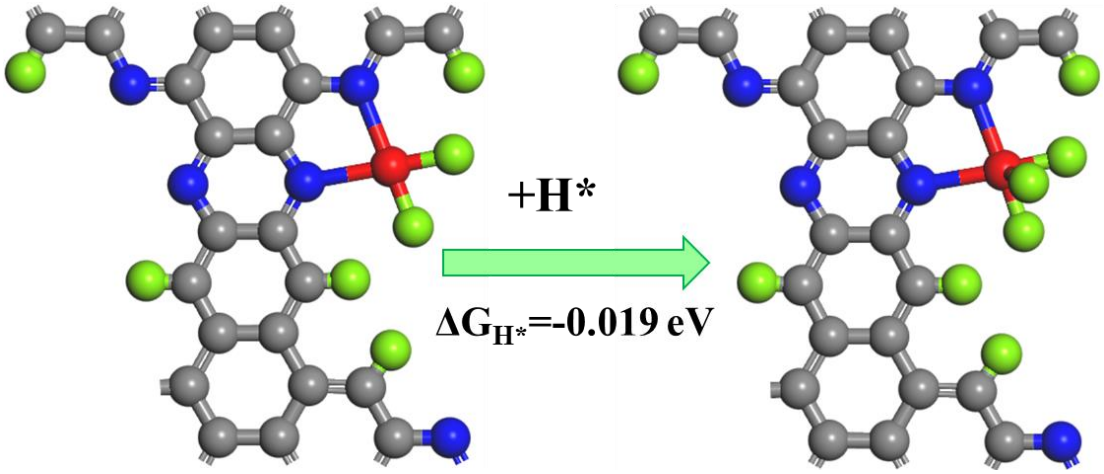

Supplementary Figure 30. Configurations of H* intermediate adsorbed on the Pt site of NGA-COF@Pt-2H.

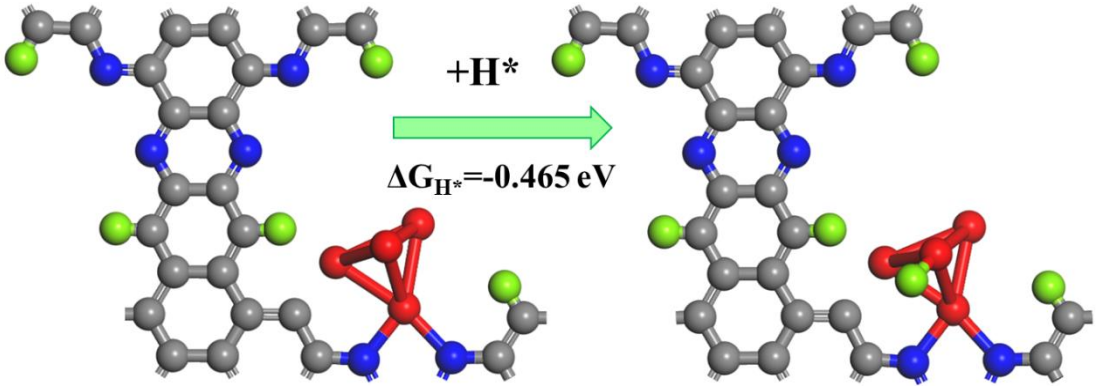

Supplementary Figure 31. Configurations of H* intermediate adsorbed on the Pt site of NGA-COF@Pt-NP.

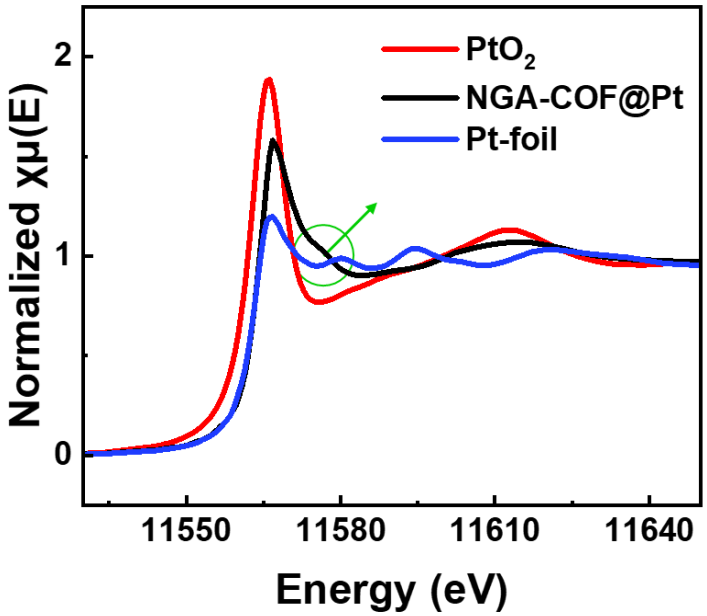

Supplementary Figure 32. Pt L_3-edge XANES spectra of Pt-foil, NGA-COF@Pt and PtO_2.

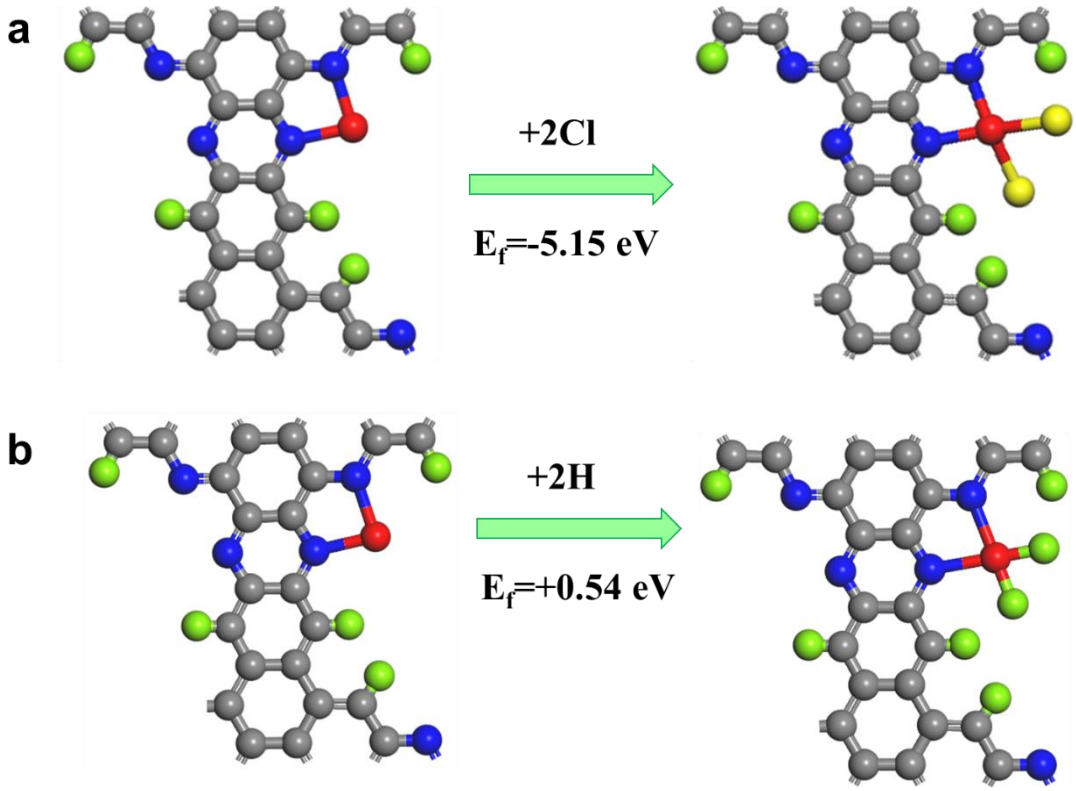

Supplementary Figure 33. Reaction path and formation energy of (a) NGA-COF@Pt to NGA-COF@Pt-2Cl and (b) NGA-COF@Pt to NGA-COF@Pt-2H.

Notes for Supplementary Figure 33: Theoretically, NGA-COF@Pt-2Cl is easier to form than NGA-COF@Pt-2H from NGA-COF@Pt. Therefore, if the real configuration of the catalyst before the Zeta potential test is NGA-COF@Pt, it should form NGA-COF@Pt-2Cl after the test (in 1 mmol·L^{-1} KCl solution).

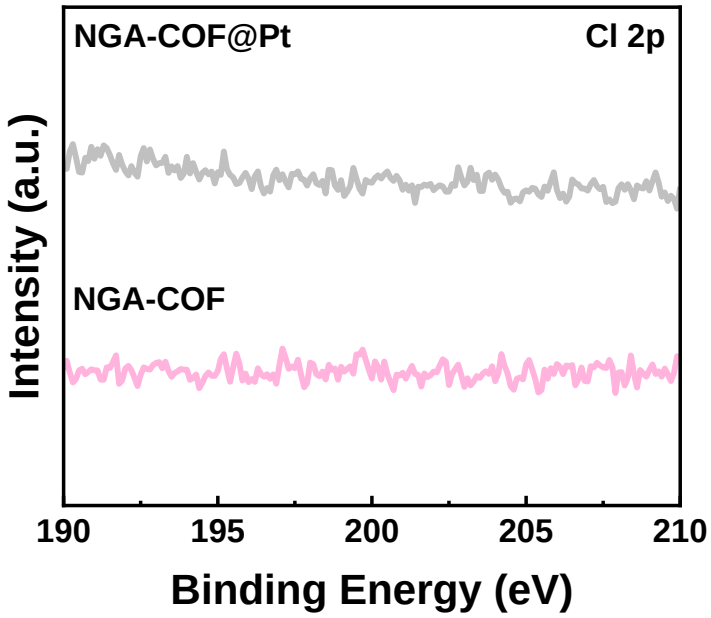

Supplementary Figure 34. High-resolution XPS spectra of Cl 2p of NGA-COF@Pt after Zeta potential test.

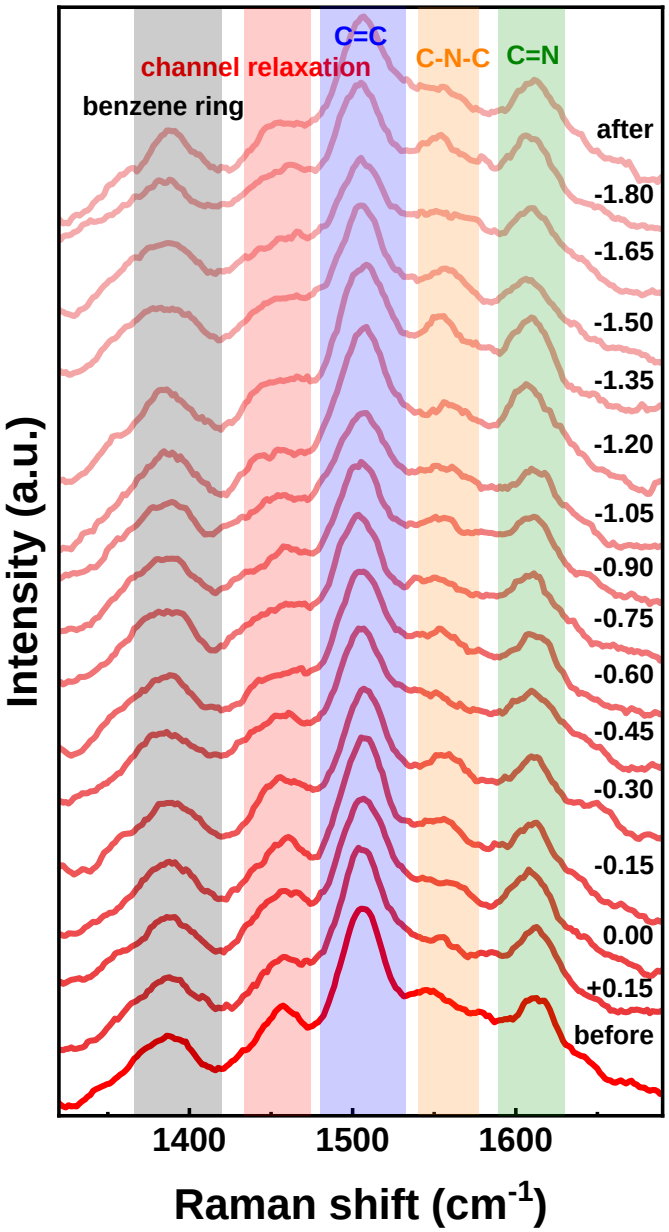

Supplementary Figure 35. In situ Raman analysis of NGA-COF@Pt during the HER process at different potentials in 1 M KCl.

Notes for Supplementary Figure 35: Chloride ions and potassium ions may affect the respiration effect of COF by filling the micropores of NGA-COF in the HER process. Therefore, some intensity fluctuations may occur in the in-situ Raman spectra including channel relaxation at 1462 cm^{-1} and C-N-C bridge vibration at 1559 cm^{-1}. These fluctuations were not observed in the previous 0.5M sulfuric acid (**Figure 5e**) because the hydrogen ion radius was too small and the sulfate ion radius was too large to fill into the micropores of NGA-COF during the HER process.

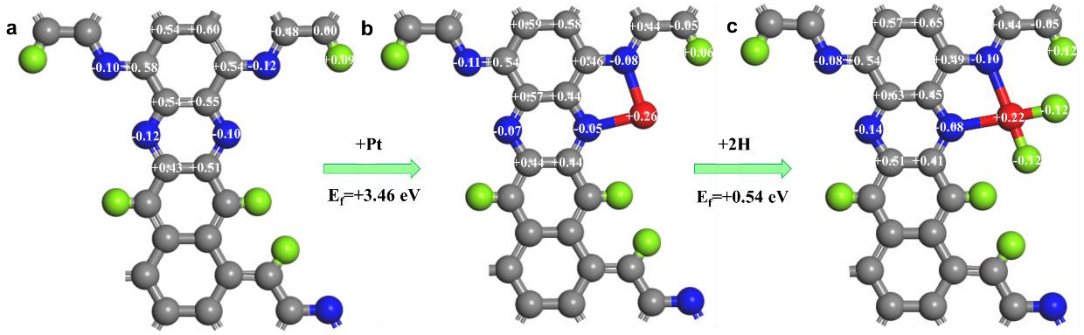

Supplementary Figure 36. Configurations of (a)NGA-COF, (b) NGA-COF@Pt and (c) NGA-COF@Pt-2H with Bader charge analysis marked on specific atoms, respectively, and the corresponding formation energy between these configurations.

Notes for Supplementary Figure 36: According to Bader charge analysis, in NGA-COF@Pt-2H, the two H atoms connected to Pt are negatively charged, which can stabilize the excess positive charge on Pt. These two negative H atoms can neutralize the excess positive charge on Pt and regulate the electronic structure of Pt. Since there is only H^+ in the electrochemically modified solution (0.5 M H_2SO_4), the two negative H atoms can only be realized at the electrochemical cathode potential applied. This also explains why the formation energy is higher than 0 eV. In addition, after two H atoms are attached, the electronic structure of N atoms and benzene ring near Pt (**Supplementary Figure 36c**) is closer to the original NGA-COF (**Supplementary Figure 36a**), which reduces the risk of structural distortion of COF caused by the introduction of Pt (**Supplementary Figure 36b**) and increases the stability of the two-dimensional structure of COF during the HER process (corroborated with the in-situ Raman spectra results).

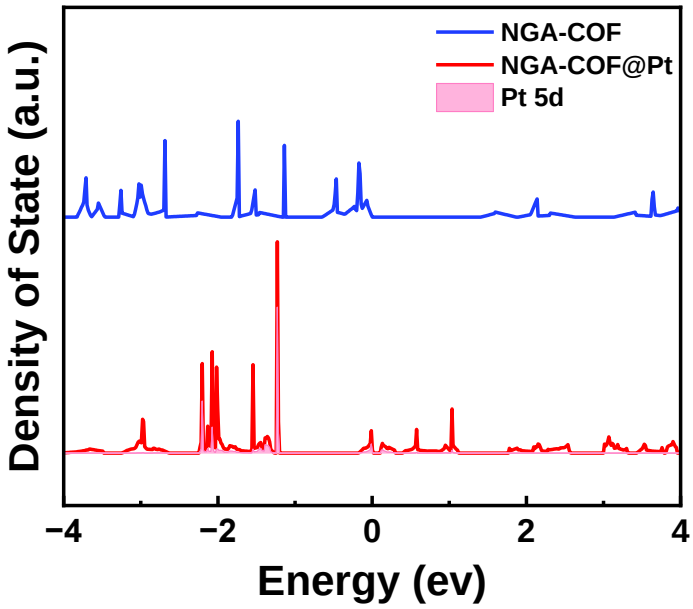

Supplementary Figure 37. Calculated TDOS of NGA-COF and NGA-COF@Pt.

Notes for Supplementary Figure 37: The narrowing of the band gap after doping of Pt single atoms is mainly due to the contribution of Pt 5d orbitals to the electronic states near the Fermi level.

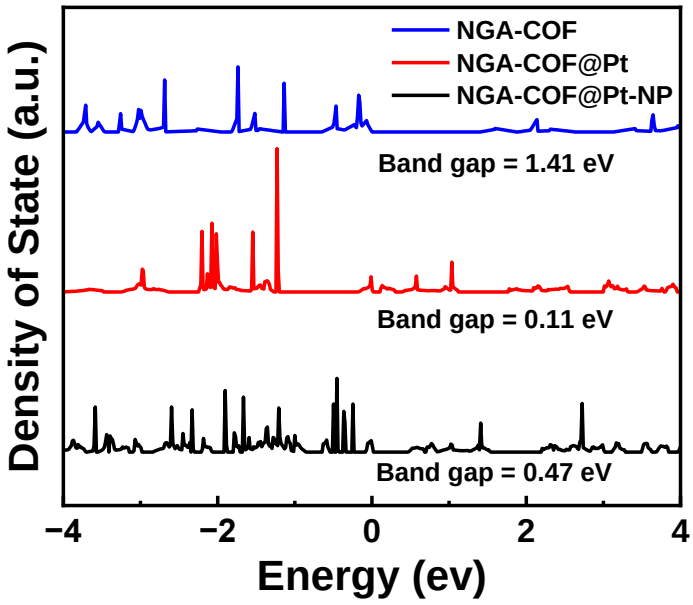

Supplementary Figure 38. Calculated TDOS of NGA-COF, NGA-COF@Pt and NGA-COF@Pt-NP.

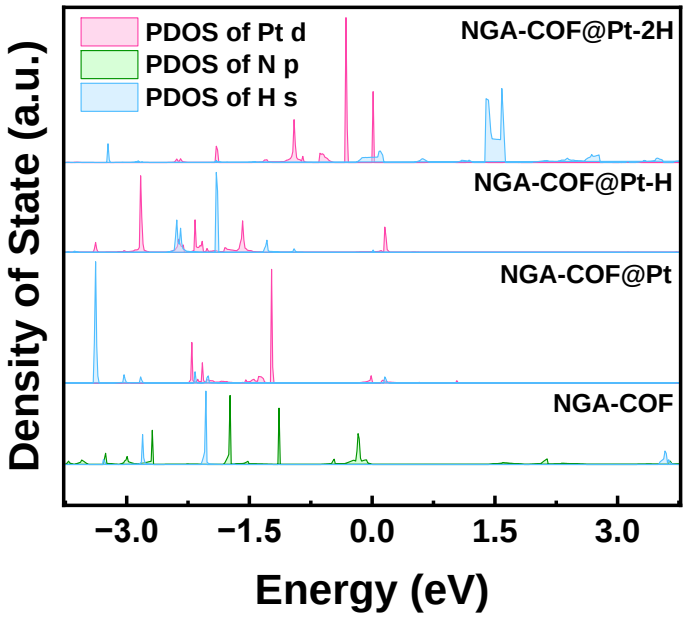

Supplementary Figure 39. Calculated PDOS of Pt d orbital (NGA-COF@Pt, NGA-COF@Pt-H and NGA-COF@Pt-2H), N p orbital (NGA-COF) and corresponding s orbital of H* intermediate interacting with them.

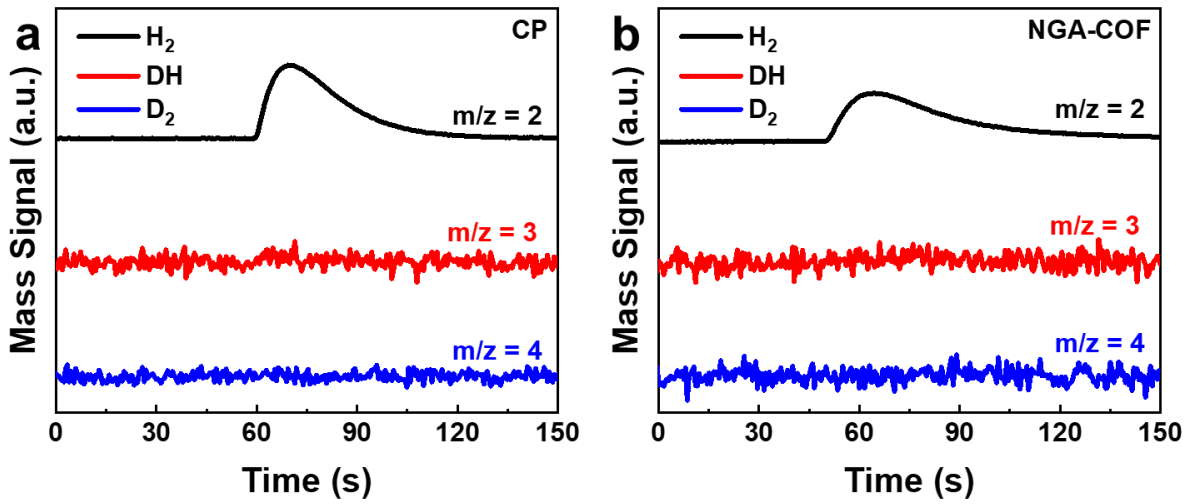

Supplementary Figure 40. DEMS measurements of H_2, DH and D_2 signals from the reaction products for D-labeled (a) CP, (b) NGA-COF.

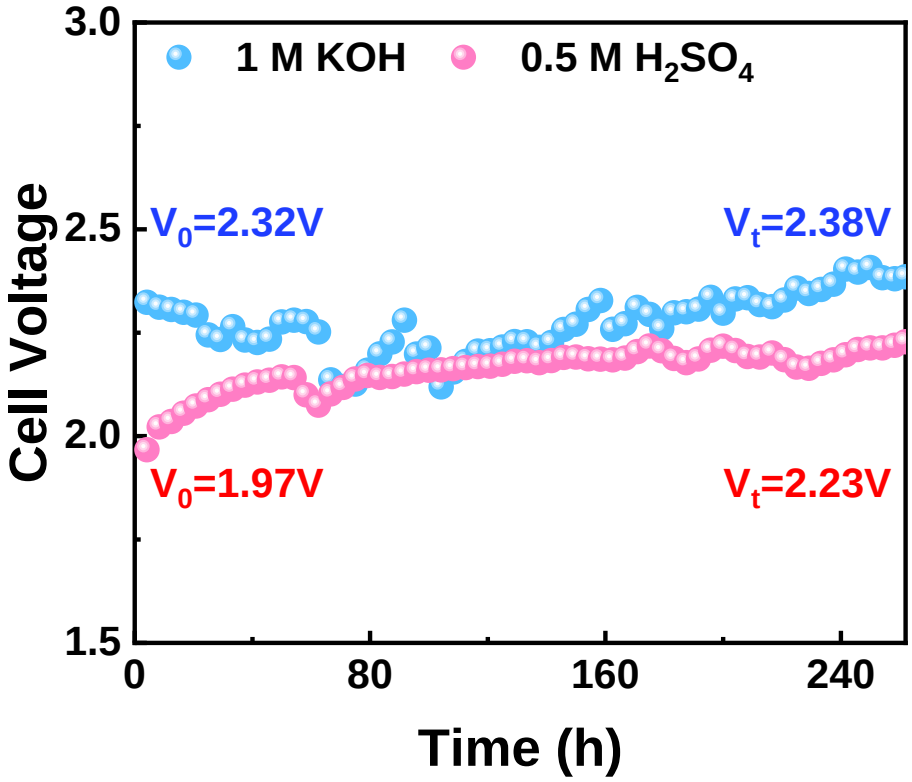

Supplementary Figure 41. Stability tests of NGA-COF@Pt-2H||RuTiIr electrode pair towards EWS in 0.5 M H_2SO_4 or 1 M KOH under simulating working condition (constant current charging, current density = 100 mA·cm^2).

Supplementary Table 1. Structural parameters obtained from the Pt L_3-edge EXAFS fitting for NGA-COF@Pt

Path	CN	R(Å)	ΔE_0(eV)	$\sigma^2(10^{-3}$ Å$^2)$	R factor
Pt-N	2	1.97±0.012	4.2±0.018	6.5±3.5	0.0147

Note for Table S1: CN is the coordination number for Pt-N path; R is interatomic distance; σ^2 is Debye-Waller factor (a measure of thermal and static disorder in absorber-scatterer distances); ΔE_0 is edge-energy shift (the difference between the zero kinetic energy value of the sample and that of the theoretical model) and R factor is degree of the fitting (The smaller the R value, the closer the fitting result is to the reality)[8].

Supplementary Table 2. Structures used for theoretical calculation in this paper and corresponding abbreviations.

	Abbreviation	Structure representation
1	NGA-COF	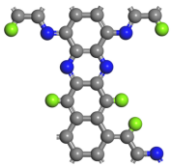
2	NGA-COF@Pt	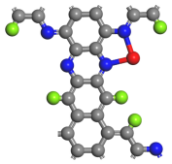
3	NGA-COF@Pt-H	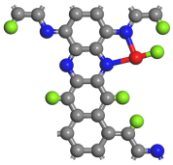
4	NGA-COF@Pt-2H	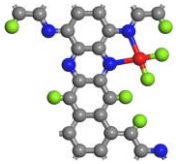
5	NGA-COF@Pt-3H	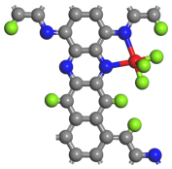
6	NGA-COF@Pt-NP	
7	NGA-COF@Pt-2Cl	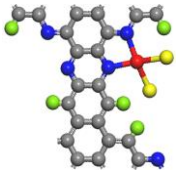
8	NGA-COF@Pt-N_4	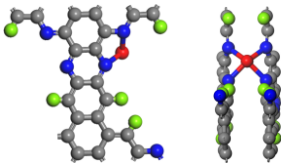

Supplementary Table 3. Comparison of noble materials electrocatalytic HER performances in acidic electrolyte.

Electrocatalysts	η_{10} (mV)	η_{100} (mV)	Tafel slop (mV dec^{-1})	Mass activity ($A \cdot g^{-1}$)	TOF (s^{-1})	Ref.
Pt_1/N-C	19	36	14.2	N/A	22.07~η_{50}	9
IrCo@N-C	24	100	23	N/A	N/A	10
$Mo_2TiC_2T_x$-Pt_{SA}	30	77	30	8300~η_{77}	N/A	1
Pt_{SA}/OLC	38	100~η_{55}	36	7400~η_{38}	40.78~η_{100}	11
PtN_x/TiO_2	67	N/A	34	37500~η_{50}	37.9~η_{50}	12
NM-HEA NPs	60	N/A	N/A	N/A	3.1~η_{50}	13
Ru@Ni-MOF	37	112	33	N/A	N/A	14
Ni@NiP-Ru	51	95~η_{65}	35	N/A	1.1~η_{100}	15
Pt_{SA}/m-WO_{3-x}	38	N/A	45	12800~η_{50}	35~η_{100}	16
C_3N_4–Ru	140	N/A	57	N/A	N/A	17
Pt/C	**23**	**51**	**29**	**1013~η_{44}**	**1.02~η_{44}**	**This**
NGA-COF@Pt	**13**	**35**	**22**	**18165~η_{44}**	**18.4~η_{44}**	**work**

Supplementary Table 4. Comparison of noble materials electrocatalytic HER performances in alkaline electrolyte.

Electrocatalysts	η_{10} (mV)	η_{100} (mV)	Tafel slop (mV dec^{-1})	Mass activity ($A \cdot g^{-1}$)	TOF (s^{-1})	Ref.
Pt_{SA}-NiO/Ni	26	86	27	20600~η_{100}	5.71~η_{50}	[18]
Pt_1/N-C	46	210	36.8	N/A	1.89~η_{50}	[9]
Pt_{SA}-$Co(OH)_2$	29	105	35	1600~η_{50}	N/A	[19]
IrCo@N-C	45	N/A	80	N/A	N/A	[10]
PtNi-O/C	40	105	79	7230~η_{70}	N/A	[20]
$Pt_{3.6}$Ni-S NWs	38	80~η_{80}	115	4370~η_{70}	N/A	[21]
$PtSe_2$/Pt	42	160~η_{60}	53	N/A	N/A	[22]
Rh@Pt_{2L}	5	63	30.5	32790~η_{100}	9.00~η_{100}	[23]
Ru@Ni-MOF	22	105	40	400~η_{100}	1.47~η_{100}	[14]
Pt/NiO@Ni/NF	34	110	39	532~η_{50}	2.01~η_{100}	[24]
PtC	**29**	**130**	**92**	**486~η_{50}**	**0.49~η_{50}**	**This**
NGA-COF@Pt	**17**	**52**	**24**	**5502~η_{50}**	**5.56~η_{50}**	**work**

References

1 Zhang, J. Q. *et al.* Single platinum atoms immobilized on an MXene as an efficient catalyst for the hydrogen evolution reaction. *Nat. Catal.* **1**, 985-992, (2018).

2 Chen, H. *et al.* Promoting Subordinate, Efficient Ruthenium Sites with Interstitial Silicon for Pt-Like Electrocatalytic Activity. *Angew. Chem. Int. Ed.* **58**, 11409-11413, (2019).

3 Zhang, H. B. *et al.* Dynamic traction of lattice-confined platinum atoms into mesoporous carbon matrix for hydrogen evolution reaction. *Sci. Adv.* **4**, eaao6657, (2018).

4 Cherevko, S. *et al.* Dissolution of Noble Metals during Oxygen Evolution in Acidic Media. *Chemcatchem* **6**, 2219-2223, (2014).

5 Yang, Y. *et al.* Non-precious alloy encapsulated in nitrogen-doped graphene layers derived from MOFs as an active and durable hydrogen evolution reaction catalyst. *Energy Environ. Sci.* **8**, 3563-3571, (2015).

6 Zhuang, L. Z. *et al.* Sulfur-Modified Oxygen Vacancies in Iron-Cobalt Oxide Nanosheets: Enabling Extremely High Activity of the Oxygen Evolution Reaction to Achieve the Industrial Water Splitting Benchmark. *Angew. Chem. Int. Ed.* **59**, 14664-14670, (2020).

7 Yang, S. Z. *et al.* Covalent Organic Frameworks with Irreversible Linkages via Reductive Cyclization of Imines. *J. Am. Chem. Soc.* **144**, 9827-9835, (2022).

8 Ji, S. F. *et al.* Atomically Dispersed Ruthenium Species Inside Metal-Organic Frameworks: Combining the High Activity of Atomic Sites and the Molecular Sieving Effect of MOFs. *Angew. Chem. Int. Ed.* **58**, 4271-4275, (2019).

9 Fang, S. *et al.* Uncovering near-free platinum single-atom dynamics during electrochemical hydrogen evolution reaction. *Nat. Commun.* **11**, 1029, (2020).

10 Jiang, P. *et al.* Tuning the Activity of Carbon for Electrocatalytic Hydrogen Evolution via an Iridium-Cobalt Alloy Core Encapsulated in Nitrogen-Doped Carbon Cages. *Adv. Mater.* **30**, 1705324, (2018).

11 Liu, D. B. *et al.* Atomically dispersed platinum supported on curved carbon supports for efficient electrocatalytic hydrogen evolution. *Nat. Energy* **4**, 512-518, (2019).

12 Cheng, X. *et al.* Charge redistribution within platinum-nitrogen coordination structure to boost hydrogen evolution. *Nano Energy* **73**, 104739, (2020).

13 Wu, D. S. *et al.* Noble-Metal High-Entropy-Alloy Nanoparticles: Atomic-Level Insight into the Electronic Structure. *J. Am. Chem. Soc.* **144**, 3365-3369, (2022).

14 Deng, L. *et al.* Electronic Modulation Caused by Interfacial Ni‐O‐M (M=Ru, Ir, Pd) Bonding for Accelerating Hydrogen Evolution Kinetics. *Angew. Chem. Int. Ed.* **60**, 22276-22282, (2021).

15 Liu, Y. *et al.* Ru Modulation Effects in the Synthesis of Unique Rod-like Ni@Ni2P–Ru Heterostructures and Their Remarkable Electrocatalytic Hydrogen Evolution Performance. *J. Am. Chem. Soc.* **140**, 2731-2734, (2018).

16 Park, J. *et al.* Investigation of the Support Effect in Atomically Dispersed Pt on WO3−x for Utilization of Pt in the Hydrogen Evolution Reaction. *Angew. Chem. Int. Ed.* **58**, 16038-16042, (2019).

17 Peng, Y. *et al.* Hydrogen evolution reaction catalyzed by ruthenium ion-complexed graphitic carbon nitride nanosheets. *J. Mater. Chem. A* **5**, 18261-18269, (2017).

18 Zhou, K. L. *et al.* Platinum single-atom catalyst coupled with transition metal/metal oxide heterostructure for accelerating alkaline hydrogen evolution reaction. *Nat. Commun.* **12**, 3783, (2021).

19 Zhou, K. L. *et al.* Seamlessly conductive Co(OH)(2)tailored atomically dispersed Pt electrocatalyst with a hierarchical nanostructure for an efficient hydrogen evolution reaction. *Energy Environ. Sci.* **13**, 3082-3092, (2020).

20 Zhao, Z. P. *et al.* Surface-Engineered PtNi-O Nanostructure with Record-High Performance for Electrocatalytic Hydrogen Evolution Reaction. *J. Am. Chem. Soc.* **140**, 9046-9050, (2018).

21 Liu, Z. J. *et al.* Aqueous Synthesis of Ultrathin Platinum/Non-Noble Metal Alloy Nanowires for Enhanced Hydrogen Evolution Activity. *Angew. Chem. Int. Ed.* **57**, 11678-11682, (2018).

22 Wang, Z. *et al.* PtSe2/Pt Heterointerface with Reduced Coordination for Boosted Hydrogen Evolution Reaction. *Angew. Chem. Int. Ed.* **60**, 23388-23393, (2021).

23 Guo, Y. *et al.* Pt Atomic Layers Boosted Hydrogen Evolution Reaction in Nonacidic Media. *Adv. Energy Mater.* **12**, 2201548, (2022).

24 Chen, Z. J. *et al.* Highly Dispersed Platinum on Honeycomb-like NiO@Ni Film as a Synergistic Electrocatalyst for the Hydrogen Evolution Reaction. *ACS Catal.* **8**, 8866-8872, (2018).